Summer season squall line simulations: Sensitivity of gravity waves to physics parameterization and implications for their parameterization in global climate models

Claudia Stephan *

Department of Atmospheric and Oceanic Sciences, University of Colorado, Boulder, Colorado

M. Joan Alexander

NorthWest Research Associates, Inc., CoRA Office, Boulder, Colorado

* *Corresponding author address:* Claudia Stephan, Atmospheric & Oceanic Sciences, 311 UCB, Folsom Stadium, Rm 255, University of Colorado, Boulder, CO 80309.

E-mail: claudia.stephan@colorado.edu

ABSTRACT

Gravity waves have important effects on the middle atmosphere circulation, and those generated by convection are prevalent in the tropics and summer mid-latitudes. Numerous case studies have been carried out to investigate their characteristics in high-resolution simulations. Here, the impact of the choice of physics parameterizations on the generation and spectral properties of these waves in models is investigated. Using the Weather Research and Forecasting Model (WRF) a summer-time squall line over the Great Plains is simulated in a three-dimensional, non-linear and non-hydrostatic mesoscale framework. The distribution of precipitation strength and echo tops in the simulations are compared with radar data. Unsurprisingly, those storm features are most sensitive to the microphysics scheme. However, it is found that these variations in storm morphology have little influence on the simulated stratospheric momentum flux spectra. These results support the fundamental idea behind climate model parameterizations: That the large scale storm conditions can be used to predict the spectrum of gravity wave momentum flux above the storm irrespective of the convective details that coarse resolution models cannot capture. The simulated spectra are then contrasted with those obtained from a parameterization used in global climate models. The parameterization reproduces the shape of the spectra reasonably well but their magnitudes remain highly sensitive to the peak heating rate within the convective cells.

1. Introduction

Gravity waves are an important component of the momentum budget of the middle atmosphere (Holton 1983; Andrews et al. 1987). Convection is a known source of gravity waves, and satellite observations reveal the Midwestern US as a "hotspot" for gravity waves generated by convection during the spring and summer months (Hoffmann and Alexander 2010).

Climate models cannot resolve these gravity waves, yet their forcing effects on the circulation have demonstrated importance for several climate processes. Gravity waves affect the timing of the transition in springtime from winter westerlies to summer easterlies in the stratosphere (Scaife et al. 2002), with associated effects on planetary wave and synoptic wave propagation and drag. They also play an important role in driving the mean-meridional transport circulation in the summer hemisphere that controls the transport of important radiatively-active trace gases like ozone and water vapor (Alexander and Rosenlof 2003; Okamoto et al. 2011).

These effects of small-scale gravity waves must be approximated using gravity wave parameterizations in climate models, and the parameterizations range in complexity from simple assumptions of uniform sources (Manzini and McFarlane 1998) to more complex methods that relate the spectrum of gravity waves to properties of convection in the climate model (Beres et al. 2005; Kim et al. 2013).

The parameter settings that must be chosen to apply these gravity wave parameterizations in climate models are poorly constrained by observations, so they are instead based largely on cloud-resolving model results (Beres 2004; Choi and Chun 2011). The cloud-resolving model studies themselves use parameterized physics for the microphysics of precipitation particle formation and boundary layer processes. Previous cloud-resolving model studies of gravity waves generated by convection have not explored the sensitivity of the waves generated to these physics parameterizations.

Here we test whether or not gravity wave activity is sensitive to hydrometeor distributions

and convective details that high-resolution models cannot capture with high fidelity. To this end we investigate the sensitivity of key properties of the convection in cloud-resolving model simulations to the choice of physics parameterizations in these models. The key sensitivity is not surprisingly to the choice of microphysics scheme. We further examine the sensitivity of the gravity waves above the storm to the microphysics scheme, and compare the gravity wave spectrum predicted by the Beres gravity wave parameterization against the simulated spectrum in the cloud-resolving model simulations. Finally, we investigate the potential for using precipitation radar observations for predicting the spectrum of gravity waves above convection.

This study is organized as follows: In section 2 the numerical model and set of simulations is introduced. Section 3 contains a comparison of the simulated horizontal storm structure, intensities of precipitation and storm depth with radar measurements focusing on precipitation rates and echo top heights. The simulated stratospheric momentum flux spectra and their sensitivity to microphysics parameterization is evaluated in section 4. In section 5 we compute the stratospheric spectra using the Beres parameterization and information about the simulated latent heating fields. Furthermore, we calculate simple relationships between quantities that can be observed by radar and required input parameters for the parameterization that allow us to apply the parameterization directly to radar measurements. The last section is a summary and discussion.

2. Numerical simulations

a. Domain geometry and resolution

Using the Weather Research and Forecasting Model (WRF) version 3.3.1, a summertime squall line that occurred on June 5 2005 over the Great Plains is modeled in a three-dimensional, non-linear and non-hydrostatic mesoscale simulation. This location is part of a region where over 95% of observed gravity waves were shown to be related to deep

convection at this time of the year (Hoffmann and Alexander 2010). This strong correlation between gravity waves and convection makes this area a good place to study and characterize properties of mid-latitude convective waves. Moreover, a high density of radar observations permits accurate validation of the precipitation and other storm features. Figure 1 shows observations by the Atmospheric Infrared Sounder (AIRS) instrument from the Aqua satellite overpass of this storm confirming gravity waves in the stratosphere emerge from a region chosen as the center of the simulation.

Each run is based on consecutive simulations on three nested domains centered at 34.5°N latitude and 95.5°W longitude as shown in Figure 2. The coarsest domain with a resolution of 15 km is initialized with ERA-interim (European Centre for Medium-Range Weather Forecasting Re-Analysis) data (Dee et al. 2011), which is available at six-hour intervals at a nominal resolution of 0.7°. There are 100 vertical levels extending from the ground to the model top of 10 hPa. A stretched grid is used between the surface and 775 hPa. Above this level the vertical grid spacing remains constant at 280 m in the troposphere and 470 m in the stratosphere. Unphysical wave reflection at the upper boundary is prevented by a five kilometer deep Rayleigh damping layer that contains 21 model levels. A test in which we doubled the depth of this layer to 10 km showed no discernable effects on the simulated velocity fields or spectra, indicating that the depth of the damping layer is sufficient for this study. The horizontal resolution decreases from 15 km to 3 km and ultimately to 1 km for the innermost domain, which spans 600 km×600 km. The grids are connected through a one-way nesting procedure implying that a separate forecast is done for each domain while boundary conditions are obtained from the next coarser grid every hour. The start time of all simulations is 18 UTC on June 4 2005, which allows for nine hours of spin-up time (typical for this type of simulation) in advance of the five-hour period, 3-8 UTC on June 5 2005, during which the waves observed by AIRS were likely generated. We intend to use AIRS satellite data in future work to validate the stratospheric gravity wave spectrum generated by this storm. Since the satellite passes the region of interest around 8 UTC we focus on

the time interval between 3 and 8 UTC.

One of the strengths of the WRF model is its high effective resolution, defined as the wavelength where the model's energy spectrum decays relative to observed mesoscale spectra (Skamarock 2004). We have computed the effective resolution of our model to be 7-8 km which is consistent with the Skamarock (2004) result of $7\Delta x$.

b. Physics parameterizations

Our initial tests of the sensitivity of key storm characteristics to physics parameterizations included simulations using different boundary layer schemes, cumulus schemes on the outer coarse grid, and microphysics schemes on the inner grids. Not surprisingly, the simulated storm characteristics were most sensitive to the microphysics scheme.

We therefore designed five ensembles of simulations that differ in their microphysics schemes. These schemes are the Morrison scheme (MOR, Morrison et al. (2009)), the WRF Single-Moment 6-class scheme (WSM6, Hong and Lim (2006)), the WRF Double-Moment 6-class scheme (WDM6, Lim and Hong (2010)), the new Thompson et al. scheme (TOM, Thompson et al. (2008)) and the Milbrandt-Yau Double-Moment 7-class scheme (MY, Milbrandt and Yau (2005)). Within an ensemble, variation between individual runs is achieved by employing different planetary boundary layer (PBL) schemes and cumulus schemes. Table 1 lists the individual runs with their respective parameterizations on all domains.

The microphysics scheme is responsible for explicitly resolved vapor, cloud and precipitation processes, computing latent heat release and absorption, respectively, and modeling microphysical processes like aggregation, accretion, growth and fall-out. The microphysics schemes used here vary greatly in their level of complexity and their properties are summarized in Table 2. Within each ensemble the same microphysics scheme is used on the 3 km and 1 km domains. We found that switching the microphysics scheme on for the 15 km domain has negligible effect on results in the 1 km domain.

Cumulus schemes parameterize sub-grid scale effects due to unresolved convection. They

provide the convective component of rainfall as well as vertical heating and moisture profiles. Every ensemble contains three simulations, one each using the Kain-Fritsch (Kain and Fritsch 1990), Betts-Miller-Janjic (Betts 1986; Betts and Miller 1986) and Grell-3 (improved version of the Grell-Devenyi scheme (Grell and Devenyi 2002)), active on the 15 km domain. While the cumulus scheme affects temperature and humidity profiles over the full extent of the lower atmosphere, the planetary boundary layer scheme is key in determining thermodynamic conditions close to the ground. Hence, together the cumulus and planetary boundary layer schemes play a role in defining the depth and horizontal extent of convection.

Planetary boundary layer schemes assume that boundary eddies are not resolved. This assumption only breaks down for a horizontal resolution much smaller than 1 km, which is why we make use of them on all domains. In each ensemble the simulation that uses the Kain-Fritsch scheme (KF) on the 15 km domain is paired with the Yonsei University PBL scheme (YSU, Hong et al. (2006)), the Betts-Miller-Janjic (BMJ) simulation is paired with Mellor-Yamada-Janjic PBL scheme (MYJ, Janjic (1994)) and the Grell-3 (G3) simulation is paired with either one. The exception is the MY ensemble which contains only two simulations because running the MY microphysics scheme in combination with the MYJ planetary boundary layer scheme always leads to instabilities. With regard to the remaining physics choices we employ the Goddard scheme (Chou and Suarez 1999) for short-wave radiation, the Rapid Radiative Transfer Model (Mlawer et al. 1997) for long-wave radiation and the Noah Land Surface Model (Ek et al. 2003) throughout all simulations.

3. Sensitivity of convective properties to physics parameterization

a. Method of assessing convective properties

In this section we investigate the extent to which convective properties that are key to the generation of gravity waves are sensitive to the choice of physics parameterization.

Previous works have linked gravity wave properties in the stratosphere to characteristics of the storm below. Relationships have been found between the depth of the latent heating and the wave vertical wavelengths or between the frequencies of oscillation within the storm and the wave frequencies (Salby and Garcia 1987; Fovell et al. 1992; Alexander et al. 1995; Lane et al. 2001). Additional work showed the dependency of the wave response to both horizontal and vertical scales and frequencies of the heating (Holton et al. 2002; Beres 2004). Additionally, the storm can act as an obstacle to the flow at upper levels, generating waves with phase speeds matching the storm or rain cell propagation speed (Pfister et al. 1993; Chun and Baik 1998; Beres 2004; Alexander et al. 2006; Kuester et al. 2008). Linear mechanisms that describe these relationships between storm and wave characteristics underlie the existing parameterizations for convectively generated waves. In real convection as well as in a nonlinear model like the one used here, clear distinctions between different mechanisms are not possible since they are connected through nonlinearites. However, the properties of gravity waves above convection in parameterizations are still related to the spatial characteristics, depth and strength of the latent heating (Beres et al. 2005; Chun et al. 2008; Richter et al. 2010; Choi and Chun 2011). It is these variables that need to be constrained as accurately as possible as they are used to parameterize convectively generated waves in climate models.

We therefore put emphasis on the horizontal structure and intensities of the precipitation and on the depth of the storm by comparing the simulated precipitation rates and echo top heights to NEXRAD (Next Generation Radar) network measurements. The NEXRAD echo

top product provides the height of the 18.3 dBZ return, rounded to the nearest 5000 ft MSL. Using the same dBZ threshold, the simulated echo tops are calculated by the WRF Unified Post Processor (UPP) using knowledge of radar sensitivity to different hydrometeor types and size distributions (Koch et al. 2005). Full coverage of the innermost domain is obtained by combining the data from twelve NEXRAD stations into a mosaic as depicted in Figure 3. Echo tops are more likely under- than overestimated, as an echo top may lie above the highest elevation scan if the storm is close to the cone of silence. We therefore use the respective larger value in assembling the echo top mosaic. In obtaining a smooth precipitation map the fields from different stations are averaged. Given the overlap of individual radar cones this composition method should lead to a substantial reduction of echo top height uncertainties. To allow for a data comparison on the WRF grid and at WRF output times the original radar data is interpolated in space and time before it is combined. When comparing the radar composite to WRF output, all fields are coarsened to an 8 km×8 km grid, since this better matches the effective model resolution.

b. Results

The radar column in the upper part of Figure 4 shows the radar mosaic of maximum echo top heights during the two 60-minute intervals 3:10-4:10 UTC and 4:10-5:10 UTC. The panels at the bottom show the 60-minute accumulated precipitation along the southwest to northeast oriented rain band associated with the squall line. The storm is in its mature stage during the first hour (3:10-4:10 UTC) and starts to decay afterwards. Since gravity waves are forced most strongly during the developing and mature stages of the convection the storm dynamics after 4:10 UTC are expected to have less impact on the generation of gravity waves. For each ensemble the columns following the radar panel in Fig. 4 show the corresponding variables for the simulation run with the Kain-Fritsch cumulus and the Yonsei University planetary boundary layer scheme. Within one ensemble all simulations produce very similar looking echo top and accumulated precipitation maps (not shown) and Fig. 4

shows a representative sample.

Examining the echo tops, the most striking feature is the large abundance of echo top heights greater than 12 km in the TOM ensemble and the complete lack thereof in the MY ensemble. The MOR, WSM6 and WDM6 ensembles present echo tops that are more comparable to the radar measurements. The MOR simulations exhibit a connected large circular area of high echo tops whereas the WSM6 and WDM6 ensembles have very similar diagonal structures with several areas of high echo tops. With regard to rain we observe that the MOR and MY ensembles have the best match in precipitation when compared to the radar panel. The areas of strong precipitation (accumulation greater than 20 mm) and light precipitation (accumulation greater than 0.1 mm) are similar in size and structure to the radar panel. The rain bands in the WSM6 and WDM6 ensembles exhibit more wide-spread precipitation with weaker strong cores. The TOM ensemble has little precipitation overall.

We examined several column-integrated moisture variables since they may offer a physical explanation for the main differences found so far. From Figure 5 it is apparent that the TOM runs possess a very large amount of snow, whereas the MY simulations exhibit just the opposite tendency, less snow than average. Furthermore, whereas the TOM runs show almost no ice, the MY simulations have the largest column integrated ice values of all ensembles. These findings are perfectly consistent with the high echo tops and low precipitation rates of the TOM ensemble as snow can be carried to high altitudes by updrafts instead of falling to the ground as precipitation. The low echo tops seen in the MY simulations are most likely tied to the production of heavy hydrometeors (hail and graupel). This reasoning is consistent with previous studies, which have shown that this scheme promotes the growth of fast falling hydrometeors, i. e. graupel and hail, due to favoring riming over deposition (Van Weverberg et al. 2012; Morrison and Milbrandt 2011).

Gravity waves are efficiently generated by strong localized convective cells. While the 60-minute maps serve to detect major similarities and differences in the storm structure they may obscure those events. Figure 6 is based on 10-minute data and therefore better

takes the intermittency of convection into account. The upper panels show the amount of precipitation that fell between 3:10 and 5:10 UTC as a function of 10-minute precipitation rate. The black curve shows the ensemble mean and the orange shading indicates the range present in each ensemble. For better comparison the radar histogram is overplotted in red. The MOR simulations and even the TOM simulations that otherwise have very little precipitation possess localized events of precipitation rates greater than 20 mm/10 minutes. Overall, the MOR simulations compare best, especially at precipitation rates that exceed 14 mm/10 minutes. The MY simulations both lack strong precipitation. The WSM6 and WDM6 ensembles are similar to each other but underestimate heavy precipitation, which seems to be a general tendency in all ensemble members.

The bottom panels of Fig. 6 show the occurrence frequency of the respective cloud and echo top heights for the same time interval. The solid histogram depicts the ensemble mean and the shading shows the range. The radar distribution has a mode at 9-10 km with 10% of the values falling into this height interval. In agreement with Fig. 4 the MY simulations have no echo tops above 12 km whereas the TOM simulations exhibit a large fraction of echo tops above 14 km. The MOR, WSM6 and WDM6 simulations compare relatively well to the radar measurements. In addition, the cloud top height distribution is shown. The MY and MOR simulations have extremely high clouds tops of up to 18 km. The presence of high cloud tops in the MY ensemble indicates that the storm is deeper than suggested by the shallow echo tops.

The above discussion has shown that the choice of microphysics parameterization can lead to substantial differences in the distributions of local precipitation rates, particularly in the occurrence of intense localized cells. Since localized intense cells have been observed as intense gravity wave sources, we next compare the spectrum of stratospheric gravity waves among the different simulations.

4. Sensitivity of the stratospheric momentum flux spectrum and forcing to physics parameterizations

In the previous section we have described the sensitivity of echo and cloud top height as well as rain rates to the choice of microphysics parameterization. The depth and amplitude of the heating are important parameters that determine the amplitude and shape of the stratospheric momentum flux spectrum. The wind profile above the heating region also plays an important role as critical level filtering leads to dissipation. This occurs when a wave approaches a level where the phase speed equals the wind speed. In all simulations there is a level of strong shear present in both the zonal and meridional direction as can be seen in Figure 7. In this section we will examine the modeled stratospheric momentum flux spectra and investigate the spectrum's sensitivity to the choice of microphysics parameterization. Details on the computation of the spectra can be found in Appendix A. Figure 8 shows ensemble-averaged momentum flux spectra computed from the simulations as a function of phase speed and propagation direction at 95 hPa. Below each spectrum the domain- and time-mean (550 km$\times$550 km and five hours) momentum flux integrated over all angles and phase speeds is shown. The ensemble mean is shown in black and the red numbers denote the minimum and maximum integrated flux of the individual runs in the respective ensemble. We notice that these spectra look remarkably similar in terms of both their shape and magnitudes despite differences in the associated tropospheric storm structure. The MY simulations have a distinctively high momentum flux relative to the other ensembles, which is consistent with larger maximum heating rates as will be shown in section 5. The minima in the momentum flux spectra that appear as holes in the NE quadrants of Fig. 8 are caused by wind filtering in the upper troposphere.

Dissipation of momentum flux due to processes like background wind filtering leads to a force on the mean flow. With regard to the parameterization of gravity waves in GCMs this quantity is particularly important. The domain- and time-mean zonal and meridional force

per unit mass due to the vertical gradient in zonal and meridional momentum flux is given by $[a_x, a_y] = -\frac{1}{\rho_0}\frac{\partial}{\partial z}\left[\rho_0\overline{u'w'}, \rho_0\overline{v'w'}\right]$. For the computation of the vertical gradient we have to take into account that some waves leave the domain. The expressions for this boundary flux correction, equations B18 and B19, are derived in Appendix B.

Figure 9 shows the mean forcing for each ensemble. The boundary flux correction is shown in green and the corrected net forcing in red. The boundary flux effect below 80 hPa is as large as -1 m/s/day but decreases rapidly with altitude. The strong westward zonal force in the lower stratosphere seen in each ensemble is associated with the westward shear (Fig. 7) that causes dissipation of westward propagating waves. Similarly, the southward force peaking near 60 hPa is associated with the southward shear at this level. The panel on the right of Fig. 9 overlays the net-forcings to allow for a better comparison. The variability between these curves is of the same order of magnitude as the variability within each ensemble (not shown).

The differences in storm structure seen in echo top height, cloud top height and precipitation caused by different microphysics schemes are substantial. The heating amplitude, which is related to the amount of precipitation, the heating depth and horizontal width of the convective cells are crucial parameters that determine the spectrum above convection in convective gravity wave source parameterizations. If we assume that linear theory, the basis for these GCM parameterizations, provides an accurate first order approximation for the stratospheric gravity waves, there is good reason to expect significant differences between the momentum flux spectra examined in this section. However, the stratospheric momentum flux spectra and forcings do not appear to critically depend on the microphysics scheme. Instead we observe similar wave amplitudes, wave spectra and mean flow forcing profiles between any two simulations. This finding is promising for the formulation of GCM parameterizations: A reasonably accurate forecast of the gravity wave spectrum should be possible despite uncertainties in the hydrometeor distributions.

In the next section we examine how a GCM parameterization responds to changes in input

parameters that are derived from the convective vertical heating profiles of the simulations.

5. Comparison of parameterized and simulated spectra

The Beres parameterization (Beres et al. 2004; Beres 2004) is based on linear theory and assumes a heating field that has a Gaussian horizontal distribution with a full width at half maximum of $2\sqrt{\ln 2}\sigma_x$ and $2\sqrt{\ln 2}\sigma_y$ and a half sine distribution in the vertical which is determined by the heating height h and the amplitude $Q_{\max}$ of the heating profile. Other required input variables are the frequency distribution of the heating, the mean wind in the heating region (ground to height h) and the minimum and maximum zonal and meridional wind components between the top of the heating region and the level of interest. The latter information is needed to correct for critical level filtering.

In Beres et al. (2004) it was shown that the assumption of a red frequency spectrum leads to results that are almost indistinguishable from using the true frequency distribution found in convection. Heating depth h and maximum heating $Q_{\max}$ are derived every 10 min from the heating profile averaged over convective pixels. We define a grid point as convective when the 10-min heating exceeds .004 K/s anywhere in the column. This value is typical for heating rates in squall lines (Beres 2004). The ensemble-mean vertical heating profiles averaged over all convective pixels and the time interval 3:10-5:10 UTC are shown in Figure 10. In averaging individual vertical profiles both positive and negative heating rates are combined. The heating depth h is determined every ten minutes by identifying the height where the vertical profile decays to 10% of $Q_{\max}$. Linear interpolation in height is applied when this value is located between two model levels. Fig. 10 also shows the average convective fraction (CF) over the first two hours. This quantity varies from 5% of the domain for the MY ensemble to 14% for the WDM6 ensemble.

Finally, the widths of the heating cells in the simulations are very variable and we assume a size of $\sigma_x = \sigma_y = 1500$ m to match the value used in Beres et al. (2005), where this pa-

rameterization was implemented in the Whole Atmosphere Community Climate (WACCM) model. Increasing the horizontal size of a heating cell in the parameterization leads to a broader phase speed distribution. Given the specific wind profile in our study this results in a larger integrated flux as wind filtering impacts a relatively smaller fraction of the spectrum. For example, a test with doubled σ_x and σ_y from 1500 m to 3000 m gives an increase in integrated flux of a factor of about 2.

Figure 11 shows the distribution of maximum column heating exceeding the convective threshold of .004 K/s for run MOR1 at 3:10 UTC. All other simulations show a similar structure of a southwest to northeast oriented squall line with organized small convective cells. The required winds for the parameterization are computed from the domain-averaged wind profiles at each time.

The left panel in Figure 12 shows the parameterized spectrum averaged over all simulations and the time interval 3:10 to 8:00 UTC. We examined the parameterized spectrum using differing values of h, $Q_{\max}$, and CF varying every 10 min for the different simulation ensembles, but found the spectrum shape to be virtually the same for all. The total flux obtained when integrating the spectrum over all angles and phase speeds ranges from 7.14 mPa to 30.77 mPa among the ensemble members with a mean of 13.88 mPa. This variability is mainly caused by differing values for $Q_{\max}$, the heating rate input to the parameterization. Comparing to Fig. 8 we notice that the general shape of the spectrum is remarkably similar given that this relatively simple parameterization cannot be expected to reproduce the details of the simulated spectra.

One concern is that the AIRS observations (Fig. 1) show waves from this storm propagating northeast, while the peak in the parameterized spectrum at low northeastward phase speeds is unlikely to survive the wind shear in the lower stratosphere. Since the AIRS observations are much higher in altitude than we have simulated, it is possible that we are seeing the small high phase speed part of the NE spectrum in AIRS whereas the rest of the spectrum of waves has either been filtered by the winds or refracted to shorter vertical

wavelengths that are not visible to the AIRS sensor. The present results cannot definitively say, but we hope to address this in future work.

Finally, we will compute the spectrum using parameters derived from the radar data itself. Since we do not have knowledge of the heating distribution, we use relationships derived from the simulations. From the radar we observe rain rates, echo tops, and fractional area of convective rain. In the simulations, we correlate these variables with heating rate, heating depth, and convective fraction, respectively. Figure 13 shows the correlations. In finding the relationships between the height h and echo tops and between the convective fraction and rain rate we only use information from the MOR, WSM6 and WDM6 ensembles as these exhibit rain rates and echo tops that better compare to the radar measurements.

We again assume the Beres et al. (2004) red frequency spectrum and a cell size of $\sigma_x = \sigma_y = 1500$ m. To calculate the wind we use the mean profile of all ensembles. These profiles and their evolution in time is shown in Figure 14. The resulting half-sine shaped heating profile averaged over the time interval 3:10-5:10 UTC is shown in the right panel of Fig. 10 and the calculated spectrum is displayed in Fig. 12. The total flux computed from the radar data is 16.16 mPa and therefore slightly larger than the average over all simulations. This is somewhat expected because strong precipitation cells persist for a longer time in the radar observations than in the models, as can be seen in the 4:10-5:20 UTC panel of Fig. 4.

6. Conclusion and discussion

In comparing five ensembles of WRF simulations we have found that the microphysics scheme has a large impact on precipitation rates and storm depth. The simulated stratospheric momentum flux spectra, however, show similar wave amplitudes, wave spectra and mean flow forcing profiles among the simulations. These similarities support the fundamental idea behind climate model parameterizations: That the large scale storm conditions can be used to predict the spectrum of gravity wave momentum flux above the storm irrespective

of details in the hydrometeor distributions.

The input parameters to the Beres parameterization were estimated directly from the simulated latent heating rate and also from radar measurements. In both cases the parameterization reproduces the general shape of the simulated spectra reasonably well. The magnitude of the simulated spectra is highly sensitive to the peak heating rate. An accurate estimate of the heating rate within a typical convective cell is crucial and will remain a challenge in climate models where the only known quantity is the grid-mean heating profile. On the other hand, this remaining challenge supports the current practice of tuning parameterized amplitudes to obtain a desired circulation in the model. The problem of unresolved local heating rates will persist in more sophisticated parameterizations and since computational capacity will remain limited in the foreseeable future, it appears questionable that a higher level of complexity is desirable. However, some caution is warranted before generalizing the conclusions of this study to the global problem of gravity wave effects on the circulation.

It is necessary to study different storm types and different environmental wind conditions. In this midlatitude case the mean mesoscale wind profile has an important effect on the spectrum shape and this wind profile is nearly identical in all our simulations. It is conceivable that the gravity wave spectrum may be more sensitive to the microphysics scheme in other wind conditions as in the tropics.

Uncertainties also exist in the relationships between radar measurements and input parameters for the Beres parameterization (Fig. 13), as they are based on simulations of a single storm case. While the present study demonstrates the potential for using radar observations to predict the spectrum of gravity waves above the storm, additional cases need to be examined to generalize these results.

Acknowledgments.

The authors would like to thank the anonymous reviewers for their valuable comments and suggestions to improve the quality of the paper. This work was supported jointly by

409 the National Science Foundation's Physical and Dynamic Meteorology and Climate and
410 Large-scale Dynamics Programs, grant number AGS-1318932.

APPENDIX A

Computation of momentum flux spectra

The nesting procedure causes boundary waves along the edges of the innermost domain. In order to exclude these waves in the spectral analysis we truncate the domain to 550 km ×550 km by cutting off areas that lie within 10 km of the northern and eastern boundaries and 40 km of the western and southern boundaries. Using 10-minute model output between 3:10 and 8:00 UTC we compute $\tilde{u}'(k,l,f)$, $\tilde{v}'(k,l,f)$ and $\tilde{w}'(k,l,f)$ using a fast Fourier transformation (FFT). Here, $\tilde{u}'$, $\tilde{v}'$ and $\tilde{w}'$ denote the Fourier transforms of the perturbation zonal, meridional and vertical velocity components (u', v', w'), respectively. The horizontal wave numbers and wave frequency are denoted by k, l and f.

Perturbations of zonal and meridional wind were computed by subtraction of a large scale background field: For the zonal and meridional velocity, linear trends are computed along the zonal direction, the meridional direction and in time. Horizontal trends are then smoothed in two dimensions with a smoothing scale of 150 km. We verified that this design leads to very periodic perturbations and smooth background fields.

Finally, the cospectra of u' and w' and v' and w' are obtained as

$$[\mathrm{cosp}_{u'w'}(k,l,f), \mathrm{cosp}_{v'w'}(k,l,f)] = \frac{1}{\mathrm{d}k}\frac{1}{\mathrm{d}l}\frac{1}{\mathrm{d}f} \times [\tilde{u}'(k,l,f), \tilde{v}'(k,l,f)]\, \tilde{w}'^{*}(k,l,f) \quad . \qquad \text{(A1)}$$

The quantities $\rho(z) \sum_{k,l,f} [\mathrm{cosp}_{u'w'}, \mathrm{cosp}_{v'w'}]\, \mathrm{d}k\mathrm{d}l\mathrm{d}f = \rho(z) \left[\overline{u'w'}, \overline{v'w'}\right]$, are the domain- and time-mean vertical flux of horizontal and meridional momentum in $\mathrm{kgm^{-1}s^{-2}} = \mathrm{Pa}$. To obtain this quantity as a function of propagation direction and phase speed we re-bin $\mathrm{cosp}_{u'w'}(k,l,f)$ and $\mathrm{cosp}_{v'w'}(k,l,f)$ accordingly.

APPENDIX B

Computation of boundary flux

An expression for the boundary flux, i. e. the flux due to waves that propagate horizontally out of the domain can be derived from the principle of wave action conservation. An analogous calculation has been performed for a two-dimensional framework with only one horizontal dimension in Alexander and Holton (1997). Here, we extend the formalism to three dimensions. The derivation will be performed for a single propagation direction but is generalized easily by summing over all propagation angles.

For a slowly varying basic state and for steady (time-averaged) waves the wave activity $A = \sqrt{k^2 + l^2}E/\hat{\omega}$ is conserved:

$$\frac{\partial}{\partial x}\left\langle c_{gx}A\right\rangle + \frac{\partial}{\partial y}\left\langle c_{gy}A\right\rangle + \frac{\partial}{\partial z}\left\langle c_{gz}A\right\rangle = 0 \tag{B1}$$

The angle brackets denote a time average, $\hat{\omega}$ is the intrinsic frequency and $\vec{c_g}$ is the group velocity. The total energy E is given by the sum of the kinetic and the potential energy KE and PE, respectively. Expressing the perturbation velocity as $(u', v', w') = (\hat{u}, \hat{v}, \hat{w})\exp[\mathrm{i}(kx + ly + mz - \omega t)]$ and using the polarization relations

$$\hat{u} = \frac{-k}{k^2 + l^2}m\hat{w}; \quad \hat{v} = \frac{-l}{k^2 + l^2}m\hat{w} \tag{B2}$$

the kinetic energy reads

$$\mathrm{KE} = \frac{1}{2}\rho_0\left(\overline{u'^2} + \overline{v'^2} + \overline{w'^2}\right) = \frac{1}{4}\rho_0\frac{k^2 + l^2 + m^2}{k^2 + l^2}\hat{w}^2 \quad . \tag{B3}$$

The bars denote the average over one wave cycle, which effectively introduces a factor of $1/2$. If ζ denotes the vertical displacement of an air parcel, $\mathrm{d}\zeta/\mathrm{d}t = w'$ and $\overline{\zeta^2} = \frac{1}{2}\hat{w}^2/\omega^2$. The potential energy is then given by

$$\mathrm{PE} = \frac{1}{2}\rho_0 N^2\overline{\zeta^2} = \frac{1}{4}\rho_0\frac{N^2}{\omega^2}\hat{w}^2 = \frac{1}{4}\rho_0\frac{k^2 + l^2 + m^2}{k^2 + l^2}\hat{w}^2 = \mathrm{KE} = \frac{1}{2}E \quad , \tag{B4}$$

where we used the dispersion relation for high-frequency gravity waves

$$\hat{\omega}^2 = \frac{N^2(k^2+l^2)}{k^2+l^2+m^2} \quad . \tag{B5}$$

From this we obtain the group velocities as

$$c_{gx} = \frac{\partial\hat{\omega}}{\partial k} = \frac{km^2N}{(k^2+l^2+m^2)^{\frac{3}{2}}(k^2+l^2)^{\frac{1}{2}}} \quad , \tag{B6}$$

$$c_{gy} = \frac{\partial\hat{\omega}}{\partial l} = \frac{lm^2N}{(k^2+l^2+m^2)^{\frac{3}{2}}(k^2+l^2)^{\frac{1}{2}}} \quad , \tag{B7}$$

$$c_{gz} = \frac{\partial\hat{\omega}}{\partial m} = -\frac{Nm(k^2+l^2)^{\frac{1}{2}}}{(k^2+l^2+m^2)^{\frac{3}{2}}} \quad . \tag{B8}$$

After substituting w' using Eq. B2 the zonal and meridional momentum flux reads

$$\rho_0\overline{u'w'} = -\frac{1}{2}\rho_0\frac{k^2+l^2}{mk}\hat{u}^2 \quad , \quad \rho_0\overline{v'w'} = -\frac{1}{2}\rho_0\frac{k^2+l^2}{ml}\hat{v}^2 \quad . \tag{B9}$$

These quantities can be related to $c_{gz}A$, which using Eq. B8, B4 and B5 can be written as

$$c_{gz}A = -\frac{1}{2}\rho_0\frac{m}{(k^2+l^2)^{\frac{1}{2}}}\hat{w}^2 \quad . \tag{B10}$$

By means of Eq. B2 this can be expressed as a function of u' and v':

$$c_{gz}A = \frac{(k^2+l^2)^{\frac{1}{2}}}{k}\rho_0\overline{u'w'} = \frac{(k^2+l^2)^{\frac{1}{2}}}{l}\rho_0\overline{v'w'} \tag{B11}$$

The components of the zonal and meridional force now become

$$-\frac{\partial}{\partial z}\left\langle\rho_0\overline{u'w'}\right\rangle = -\frac{k}{(k^2+l^2)^{\frac{1}{2}}}\frac{\partial}{\partial z}\left\langle c_{gz}A\right\rangle = -\cos\phi\left[-\frac{\partial}{\partial x}\left\langle c_{gx}A\right\rangle - \frac{\partial}{\partial y}\left\langle c_{gy}A\right\rangle\right] \quad , \tag{B12}$$

$$-\frac{\partial}{\partial z}\left\langle\rho_0\overline{v'w'}\right\rangle = -\frac{l}{(k^2+l^2)^{\frac{1}{2}}}\frac{\partial}{\partial z}\left\langle c_{gz}A\right\rangle = -\sin\phi\left[-\frac{\partial}{\partial x}\left\langle c_{gx}A\right\rangle - \frac{\partial}{\partial y}\left\langle c_{gy}A\right\rangle\right] \quad , \tag{B13}$$

where ϕ denotes the horizontal propagation direction. Furthermore,

$$c_{gx}A = \frac{1}{2}\rho_0\frac{1}{\cos\phi}\hat{u}^2 = \frac{1}{2}\rho_0\frac{1}{\tan\phi\sin\phi}\hat{v}^2 \quad , \tag{B14}$$

$$c_{gy}A = \frac{1}{2}\rho_0\frac{\tan\phi}{\cos\phi}\hat{u}^2 = \frac{1}{2}\rho_0\frac{1}{\sin\phi}\hat{v}^2 \quad , \tag{B15}$$

such that we obtain for the force components

$$
\begin{aligned}
-\frac{\partial}{\partial z}\left\langle \rho_0 \overline{u'w'} \right\rangle &= -\cos\phi \left[-\frac{\partial}{\partial x}\left(\frac{1}{2}\rho_0 \frac{1}{\cos\phi}\left\langle \hat{u}^2 \right\rangle \right) - \frac{\partial}{\partial y}\left(\frac{1}{2}\rho_0 \frac{\tan\phi}{\cos\phi}\left\langle \hat{u}^2 \right\rangle \right) \right] \\
&= \frac{1}{2}\rho_0 \left[\frac{\partial}{\partial x}\left\langle \hat{u}^2 \right\rangle + \frac{\partial}{\partial y}\left(\tan\phi \left\langle \hat{u}^2 \right\rangle \right) \right] \quad ,
\end{aligned}
\tag{B16}
$$

$$
\begin{aligned}
-\frac{\partial}{\partial z}\left\langle \rho_0 \overline{v'w'} \right\rangle &= -\sin\phi \left[-\frac{\partial}{\partial x}\left(\frac{1}{2}\rho_0 \frac{1}{\tan\phi\sin\phi}\left\langle \hat{v}^2 \right\rangle \right) - \frac{\partial}{\partial y}\left(\frac{1}{2}\rho_0 \frac{1}{\sin\phi}\left\langle \hat{v}^2 \right\rangle \right) \right] \\
&= \frac{1}{2}\rho_0 \left[\frac{\partial}{\partial x}\left(\frac{1}{\tan\phi}\left\langle \hat{v}^2 \right\rangle \right) + \frac{\partial}{\partial y}\left\langle \hat{v}^2 \right\rangle \right] \quad .
\end{aligned}
\tag{B17}
$$

Upon integration over dx and dy and using Stokes's theorem we obtain the final formulas, where we sum over all propagation angles.

$$
\begin{aligned}
-\frac{1}{\rho_0}\frac{\partial}{\partial z}\left\langle \rho_0 \overline{u'w'} \right\rangle = \frac{\Delta s}{L_x L_y}\frac{1}{2}\sum_{\phi} \\
\left[\sum_y \left[\left\langle \hat{u}^2_{x=L_x} \right\rangle - \left\langle \hat{u}^2_{x=0} \right\rangle \right] + \sum_x \left[\tan\phi \left\langle \hat{u}^2_{y=L_y} \right\rangle - \tan\phi \left\langle \hat{u}^2_{y=0} \right\rangle \right] \right] \quad ,
\end{aligned}
\tag{B18}
$$

$$
-\frac{1}{\rho_0}\frac{\partial}{\partial z}\left\langle \rho_0 \overline{v'w'} \right\rangle = \frac{\Delta s}{L_x L_y}\frac{1}{2}\sum_{\phi}\left[\sum_y \left[\frac{\left\langle \hat{v}^2_{x=L_x} \right\rangle}{\tan\phi} - \frac{\left\langle \hat{v}^2_{x=0} \right\rangle}{\tan\phi} \right] + \sum_x \left[\left\langle \hat{v}^2_{y=L_y} \right\rangle - \left\langle \hat{v}^2_{y=0} \right\rangle \right] \right] \quad .
\tag{B19}
$$

Here, $L_y = L_x = 600$ km denote the size of the domain, $\Delta s = 10$ km is the horizontal resolution, ϕ the propagation direction with $\phi = 0$ being eastward propagation and $\phi = 90$ being northward propagation. The perturbation zonal (meridional) velocities along the eastern and western boundaries are $\hat{u}_{x=L_x}$ and $\hat{u}_{x=0}$ ($\hat{v}_{x=L_x}$ and $\hat{v}_{x=0}$), respectively. Analogous notation is used for the southern ($y = 0$) and northern ($y = L_y$) boundaries.

To compute the terms in Eq. B18 and B19 that include the propagation direction we need to know how the total amplitude of $\hat{u}$ and $\hat{v}$ decomposes with different angles. To obtain this information a spectral analysis of u' and v' in time is performed for each boundary point. Here, we use the same velocity field that goes into the three-dimensional spectral analysis, i. e. the background has been subtracted. From $\tilde{u}(f)$ and $\tilde{v}(f)$ we know the amplitudes of u' and v' as well as the value of the propagation angle modulo 90°. The sign of the flux that leaves the domain at this point on the boundary is then determined by the sign of the co-spectrum of u' and v' at the given frequency.

REFERENCES

Alexander, M. J. and J. R. Holton, 1997: A model study of zonal forcing in the equatorial stratosphere by convectively induced gravity waves. *J. Atmos. Sci.*, **54**, 408–419.

Alexander, M. J., J. R. Holton, and D. R. Durran, 1995: The gravity wave response above deep convection in a squall line simulation. *J. Atmos. Sci.*, **52**, 2212–2226.

Alexander, M. J., J. H. Richter, and B. R. Sutherland, 2006: Generation and trapping of gravity waves from convection with comparison to parameterization. *J. Atmos. Sci.*, **63**, 2963–2977.

Alexander, M. J. and K. H. Rosenlof, 2003: Gravity wave forcing in the stratosphere: Observational constraints from UARS and implications for parameterization in global models. *J. Geophys. Res.*, **108**, doi:10.1029/2003JD003373.

Andrews, D. G., J. R. Holton, and C. B. Leovy, 1987: *Middle atmosphere dynamics*, Int. Geophy. Ser., Vol. 40. Academic, San Diego, Calif.

Beres, J. H., 2004: Gravity wave generation by a three-dimensional thermal forcing. *J. Atmos. Sci.*, **61**, 1805–1815.

Beres, J. H., M. J. Alexander, and J. R. Holton, 2004: A method of specifying the gravity wave spectrum above convection based on latent heating properties and background wind. *J. Atmos. Sci.*, **61**, 324–337.

Beres, J. H., R. R. Garcia, and B. A. Boville, 2005: Implementation of a gravity wave source spectrum parameterization dependent on the properties of convection in the Whole Atmosphere Community Climate Model (WACCM). *J. Geophys. Res.*, **110**, doi:10.1029/2004JD005504.

Betts, A. K., 1986: A new convective adjustment scheme .1. observational and theoretical basis. *Quart. J. Roy. Meteor. Soc.*, **112**, 677–691.

Betts, A. K. and M. J. Miller, 1986: A new convective adjustment scheme .2. single column tests using GATE wave, BOMEX, ATEX and arctic air-mass data sets. *Quart. J. Roy. Meteor. Soc.*, **112**, 693–709.

Choi, H.-J. and H.-Y. Chun, 2011: Momentum flux spectrum of convective gravity waves. Part I: An update of a parameterization using mesoscale simulations. *J. Atmos. Sci.*, **68**, 739–759.

Chou, M.-D. and M. J. Suarez, 1999: A solar radiation parameterization for atmospheric studies. NASA Tech. Rep. NASA/TM-1999-10460, 38 pp.

Chun, H.-Y. and J.-J. Baik, 1998: Momentum flux by thermally induced internal gravity waves and its approximation for large-scale models. *J. Atmos. Sci.*, **55**, 3299–3310.

Chun, H.-Y., H.-J. Choi, and I.-S. Song, 2008: Effects of nonlinearity on convectively forced internal gravity waves: Application to a gravity wave drag parameterization. *J. Atmos. Sci.*, **65**, 557–575.

Dee, D. P., S. M. Uppala, A. J. Simmons, P. Berrisford, P. Poli, and S. Kobayashi, 2011: The ERA-Interim reanalysis: configuration and performance of the data assimilation system. *Quart. J. Roy. Meteor. Soc.*, **137**, 553–597.

Ek, M. B., K. E. Mitchell, Y. Lin, E. Rogers, P. Grummann, V. Koren, G. Gayno, and J. D. Tarpley, 2003: Implementation of Noah land surface model advances in the National Centers for Environmental Prediction operational mesoscale Eta Model. *J. Geophys. Res.*, **108**, doi:10.1029/2002JD003296.

Fovell, R., D. Durran, and J. R. Holton, 1992: Numerical simulations of convectively generated stratospheric waves. *J. Atmos. Sci.*, **49**, 1427–1442.

Grell, G. A. and D. Devenyi, 2002: A generalized approach to parameterizing convection combining ensemble and data assimilation techniques. *Geophys. Res. Lett*, **29**, 1693, doi: 10.1029/2002GL015311.

Hoffmann, L. and M. J. Alexander, 2010: Occurrence frequency of convective gravity waves during the North American thunderstorm season. *J. Geophys. Res.*, **115**, doi:10.1029/ 2010JD014401.

Holton, J., J. Beres, and X. Zhou, 2002: On the vertical scale of gravity waves excited by localized thermal forcing. *J. Atmos. Sci.*, **59**, 2019–2023.

Holton, J. R., 1983: The influence of gravity wave breaking on the general circulation of the middle atmosphere. *J. Atmos. Sci.*, **40**, 2497–2507.

Hong, S.-Y. and J.-O. Lim, 2006: The WRF single-moment 6-class microphysics scheme (WSM6). *J. Kor. Met. Soc.*, **42**, 129–151.

Hong, S.-Y., Y. Noh, and J. Dudhia, 2006: A new vertical diffusion package with an explicit treatment of entrainment processes. *Mon. Wea. Rev.*, **134**, 2318–2341.

Janjic, Z., 1994: The step-mountain eta coordinate model: Further developments of the convection, viscous sublayer, and turbulence closure schemes. *Mon. Wea. Rev.*, **122**, 927–945.

Kain, J. S. and J. M. Fritsch, 1990: A one-dimensional entraining detraining plume model and its application in convective parameterization. *J. Atmos. Sci.*, **47**, 2784–2802.

Kim, Y.-H., A. C. Bushell, D. R. Jackson, and H.-Y. Chun, 2013: Impacts of introducing a convective gravity-wave parameterization upon the QBO in the Met Office Unified Model. *Geophys. Res. Lett*, **40**, doi:10.1002/grl.50353.

Koch, S. E., B. S. Ferrier, M. T. Stoelinga, E. J. Szoke, S. J. Weiss, and J. S. Kain, 2005: The use of simulated radar reflectivity fields in the diagnosis of mesoscale phenomena

546 from high-resolution wrf model forecasts. *11th Conf. on Mesoscale Processes/32nd Conf.*
547 *on Radar Meteor.*, Albuquerque, NM, available on AMS webpage, J4J.7.

548 Kuester, M. A., M. J. Alexander, and E. A. Ray, 2008: A model study of gravity waves over
549 hurricane Humberto (2001). *J. Atmos. Sci.*, **65**, 3231–3246.

550 Lane, T. P., M. J. Reeder, and T. L. Clark, 2001: Numerical modeling of gravity wave
551 generation by deep tropical convection. *J. Atmos. Sci.*, **58**, 1249–1274.

552 Lim, K.-S. and S.-Y. Hong, 2010: Development of an effective double-moment cloud micro-
553 physics scheme with prognostic cloud condensation nuclei (CCN) for weather and climate
554 models. *Mon. Wea. Rev.*, **138**, 1587–1612.

555 Manzini, E. and N. A. McFarlane, 1998: The effect of varying the source spectrum of a gravity
556 wave parameterization in a middle atmosphere general circulation model. *J. Geophys. Res.*,
557 **103**, doi:10.1029/98JD02274.

558 Milbrandt, J. A. and M. K. Yau, 2005: A multimoment bulk microphysics parameterization.
559 Part II:A proposed three-moment closure and scheme description. *J. Atmos. Sci.*, **62**,
560 3065–3081.

561 Mlawer, E. J., S. J. Taubman, P. D. Brown, M. J. Iacono, and S. A. Clough, 1997: Radiative
562 transfer for inhomogeneous atmospheres: RRTM, a validated correlated-k model for the
563 longwave. *J. Geophys. Res.*, **102**, 16 663–16 682.

564 Morrison, H. and J. Milbrandt, 2011: Comparison of two-moment bulk microphysics schemes
565 in idealized supercell thunderstorm simulations. *Mon. Wea. Rev.*, **139**, 1103–1130.

566 Morrison, H., G. Thompson, and V. Tatarskii, 2009: Impact of cloud microphysics on the
567 development of trailing stratiform precipitation in a simulated squall line: Comparison of
568 one- and two-moment schemes. *Mon. Wea. Rev.*, **137**, 991–1007.

569 Okamoto, K., K. Sato, and H. Akiyoshi, 2011: A study on the formation and trend of the
570 Brewer-Dobson circulation. *J. Geophys. Res.*, **116**, doi:10.1029/2010JD014953.

571 Pfister, L., K. R. Chan, and T. P. Bui, 1993: Gravity waves generated by a tropical cyclone
572 during the STEP tropical field program: A case study. *J. Geophys. Res.*, **98**, 8611–8638.

573 Richter, J. H., F. Sassi, and R. R. Garcia, 2010: Toward a physically based gravity wave
574 source parameterization in a general circulation model. *J. Atmos. Sci.*, **67**, 136–156.

575 Salby, M. L. and R. R. Garcia, 1987: Transient response to localized episodic heating in
576 the tropics. Part I: Excitation and short-time near-field behaviour. *J. Atmos. Sci.*, **44**,
577 458–498.

578 Scaife, A. A., N. Butchart, C. D. Warner, and R. Swinbank, 2002: Impact of a spectral
579 gravity wave parameterization on the stratosphere in the Met Office Unified Model. *J.*
580 *Atmos. Sci.*, **59**, 1473–1489.

581 Skamarock, W. C., 2004: Evaluating mesoscale NWP models using kinetic energy spectra.
582 *Mon. Wea. Rev.*, **132**, 3019–3032.

583 Thompson, G., P. R. Field, R. Rasmussen, and W. D. Hall, 2008: Explicit forecasts of winter
584 precipitation using an improved bulk microphysics scheme. Part II: Implementation of a
585 new snow parameterization. *Mon. Wea. Rev.*, **136**, 5095–5115.

586 Van Weverberg, K., A. M. Vogelmann, and H. Morrison, 2012: Sensitivity of idealized squall-
587 line simulations to the level of complexity used in two-moment bulk microphysics schemes.
588 *Mon. Wea. Rev.*, **140**, 1883–1907.

List of Tables

TABLE 1. Physics parameterizations: Planetary boundary layer (PBL), Cumulus (CU) and Microphysics (MP).

	15 km		3 km and 1 km	
Run	CU	PBL	MP	PBL
MOR I	KF	YSU	MOR	YSU
MOR II	BMJ	MYJ	MOR	MYJ
MOR III	G3	YSU	MOR	YSU
WSM6 I	KF	YSU	WSM6	YSU
WSM6 II	BMJ	MYJ	WSM6	MYJ
WSM6 III	G3	MYJ	WSM6	MYJ
WDM6 I	KF	YSU	WDM6	YSU
WDM6 II	BMJ	MYJ	WDM6	MYJ
WDM6 III	G3	YSU	WDM6	YSU
MY I	KF	YSU	MY	YSU
MY III	G3	YSU	MY	YSU
TOM I	KF	YSU	TOM	YSU
TOM II	BMJ	MYJ	TOM	MYJ
TOM III	G3	MYJ	TOM	MYJ

TABLE 2. Microphysics schemes and their predicted moments. The subscripts on the mass mixing ratios Q and the number concentrations N stand for cloud water, rain, snow, ice, graupel and hail. CCN stands for cloud condensation nuclei. The Morrison scheme (MOR) incorporates a switch allowing the user to either run it with graupel or hail. We choose the hail option as is recommended for continental convection.

MP scheme	Predicted mass mixing ratios	Predicted number concentrations
Milbrandt-Yau (MY)	Q_c, Q_r, Q_s, Q_i, Q_g, Q_h	N_c, N_r, N_s, N_i, N_g, N_h
Morrison (MOR)	Q_c, Q_r, Q_s, Q_i, $Q_{g/h}$	N_r, N_s, N_i, $N_{g/h}$
New Thompson (TOM)	Q_c, Q_r, Q_s, Q_i, Q_g	N_r, N_i
WSM6	Q_c, Q_r, Q_s, Q_i, Q_g	
WDM6	Q_c, Q_r, Q_s, Q_i, Q_g	N_c, N_r, CCN number

List of Figures

644 10 Ensemble-mean vertical heating rate profiles averaged over all convective pix-
645 els and the time interval 3:10-5:10 UTC. We define a grid point as convective
646 when the 10-min heating exceeds .004 K/s anywhere in the column. The
647 convection fraction (CF) shown in the diagram is defined as the fraction of
648 the domain that exceeds this threshold. All graphs are based on a horizontal
649 resolution of 1 km. The radar profile is calculated using estimated values for
650 the maximum heating amplitude and the heating height h as explained in
651 section 5. The radar profile has the half-sine shape that is assumed in the
652 Beres parameterization. 43

653 11 Map of heating rates exceeding the convective threshold of .004 K/s. Shown
654 is the 550 km×550 km large area of the innermost domain (see Appendix A).
655 Colors display the maximum heating in the column over each 1 km×1 km
656 grid cell. 44

657 12 Momentum flux spectra as a function of phase speed in m/s (radial coordinate)
658 and propagation angle produced by the Beres parameterization. The left
659 diagram results from using information about the simulated heating fields as
660 input to the parameterization and displays the spectrum averaged over all
661 simulations. Integrated flux values range from 7.14 mPa to 30.77 mPa among
662 the simulations. The right diagram results from applying the parameterization
663 to radar measurements. The angular resolution is 10° and the resolution in
664 phase speed is 1 m/s. 45

13 Scatter plots showing 10 minute data from all or selected simulations (see text). Panel a shows the relationship between domain mean precipitation (P_{dm}) and the maximum of the convective vertical heating profile multiplied by the convective fraction ($Q_{max} \times CF \equiv Q_{dm}$). Panel b shows the relationship between the heating depth (h) and the average over the 0.1% of the highest echo tops (Etop). Panel c shows the relationship between convective fraction (CF) and fraction of raining pixels (FR) with precipitation rates greater than 0.17 mm/10 minute. The straight lines are linear fits. The rain threshold of 0.17 mm/10 minutes in panel c (based on a resolution of 8 km ×8 km) is chosen to obtain a slope of one for the linear fit. The linear fits are used to obtain parameterization input parameters (h, CF, and Q_{dm}) from 8 km× 8 km radar precipitation and echo top fields. More information on the definition of CF, h and Q_{max} can be found in the text. 46

14 Domain-mean zonal and meridional wind profiles at 10 min intervals averaged over all simulations. These are used to calculate the winds in and above the heating region as input to the Beres parameterization for the "Radar" spectrum in Fig. 12. 47

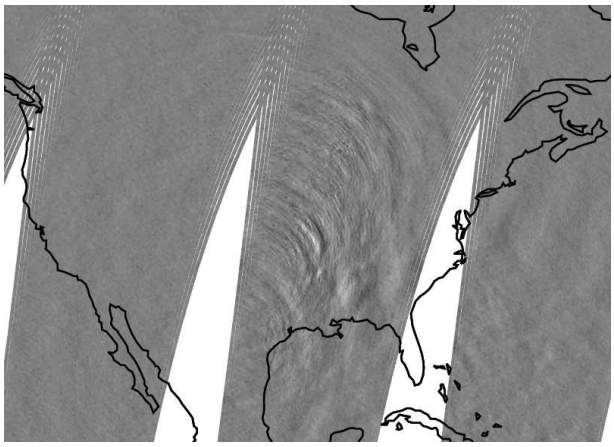

FIG. 1. Observed gravity waves in the stratosphere. The shading shows satellite brightness temperature anomalies, computed from AIRS 4.2 micron radiances as described in Hoffmann and Alexander (2010). These are descending orbit swaths with an equatorial crossing time of 1:30 am local time on 5 June 2005. Anomalies range ±2.1 K. The contour shows the North American coastline.

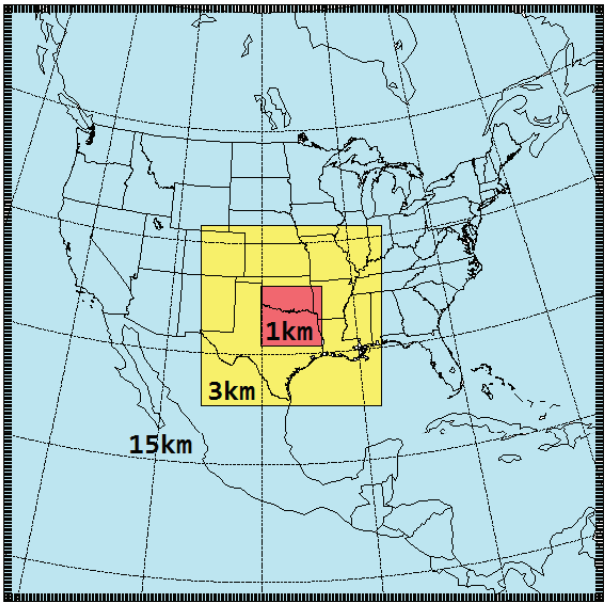

FIG. 2. Map showing the location of the three nests. Labels indicate the respective horizontal grid resolution.

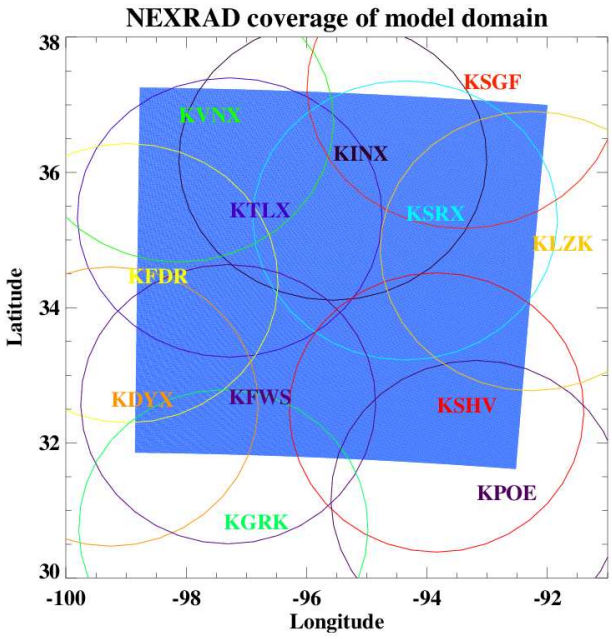

FIG. 3. Radar stations used to make the composite of echo top and precipitation fields. The four-letter identification code indicates the location and the circles the 230 km radius of individual stations. The 1 km×1 km WRF domain is depicted in blue.

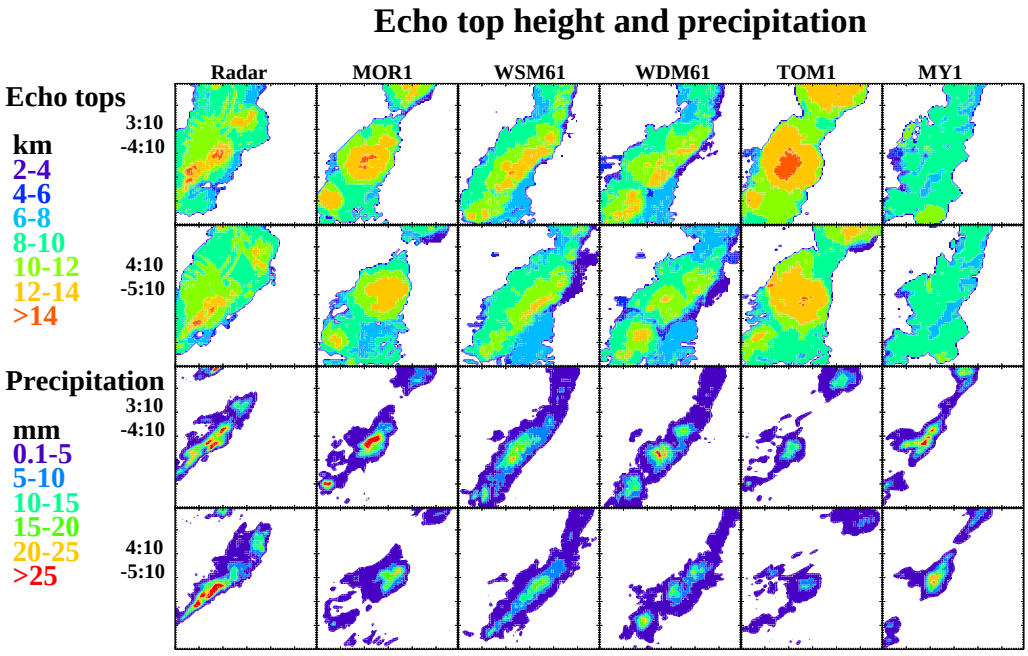

FIG. 4. The top two rows show the maximum echo top height reached during the hour and the bottom two rows the 60-minute accumulated precipitation. Each panel represents the area of the innermost model domain spanning 600 km×600 km. Rows are labeled with the hour in UTC. The left column contains radar measurements and the other columns display simulated values from selected model runs. All plots are based on a horizontal resolution of 8 km which roughly corresponds to the model effective resolution.

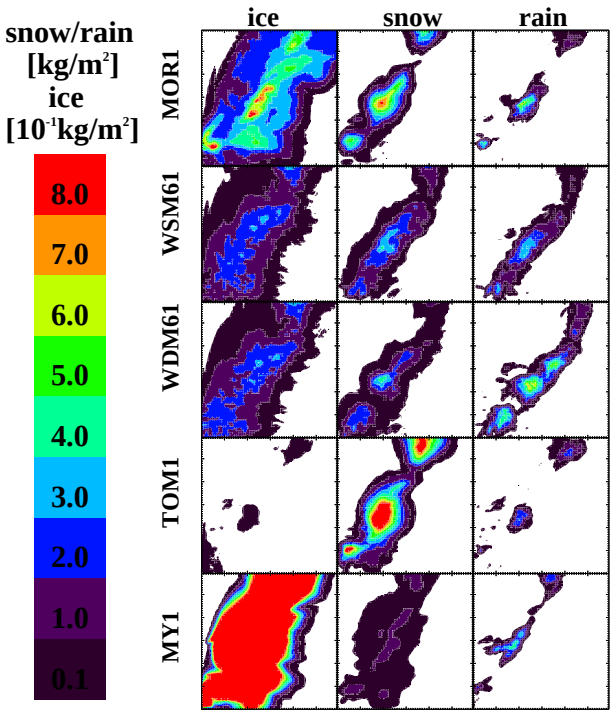

FIG. 5. Column integrated ice, snow and rain over the inner domain at 3:10 UTC. Each row represents a different simulation. All plots are based on a horizontal resolution of 8 km.

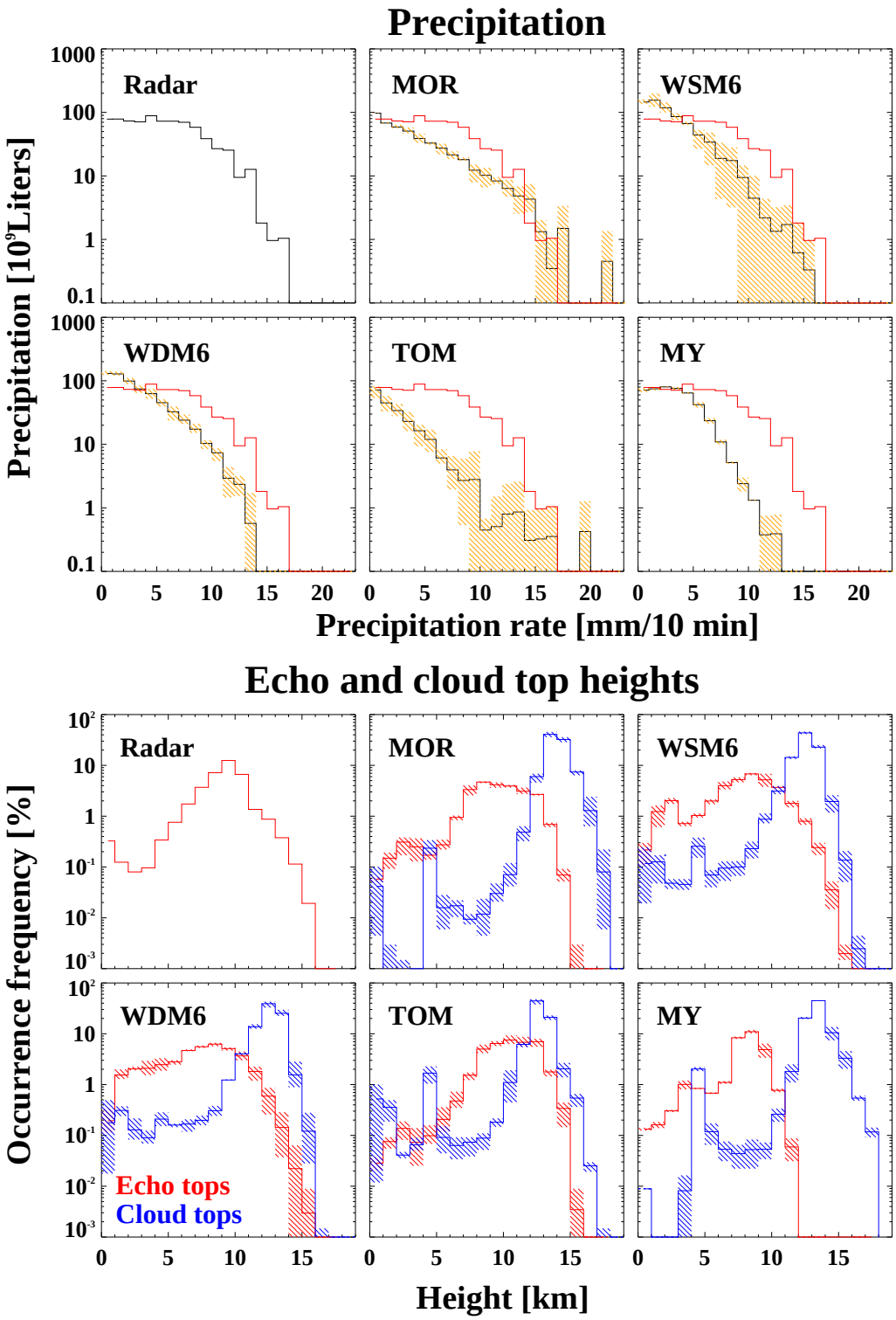

FIG. 6. Distribution of precipitation (top part of the figure) and echo top and cloud top height (bottom part of the figure) from the five ensembles and radar data. All data is based on 10-minute time intervals ranging from 3:10 to 5:10 UTC and a horizontal resolution of 8 km. Solid histograms denote the ensemble mean and shading denotes the range of values within an ensemble. In the precipitation plots the radar histogram is overlaid in red.

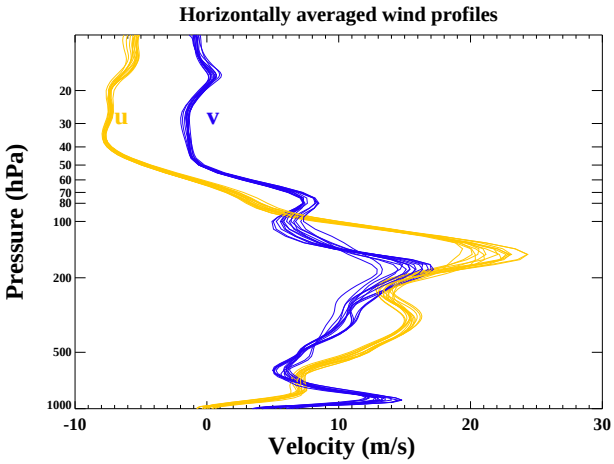

FIG. 7. Zonal (yellow) and meridional (blue) vertical wind profiles averaged over the inner domain and the time interval 3:10-8:00 UTC. A separate line is drawn for each of the 14 simulations.

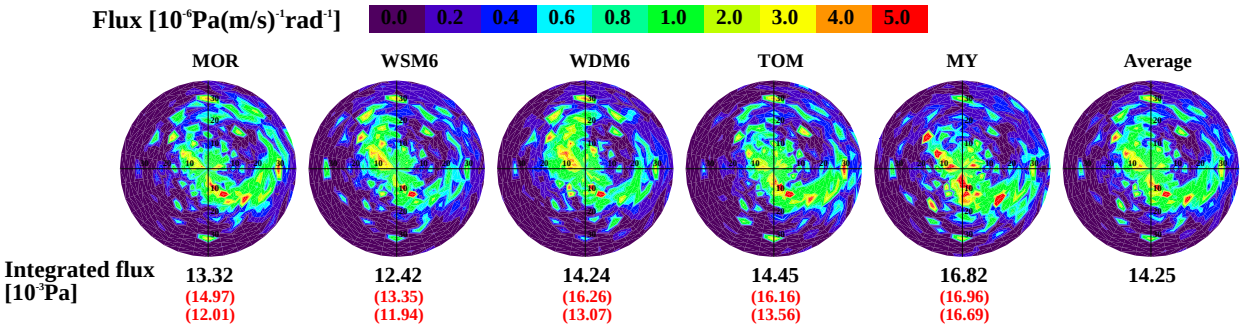

FIG. 8. Ensemble-mean momentum flux spectra at 95 hPa as a function of phase speed (radial coordinate) and propagation angle for the five ensembles. Phase speed values range from 0 to 39 m/s. The angular resolution is 10° and the phase speed resolution is 2 m/s. Northward is at the top and eastward right in each plot. The rightmost spectrum shows the average over all ensembles. The black numbers denote the total flux integrated over all phase speeds and propagation angles. The red numbers denote the maximum and minimum integrated flux value of each ensemble.

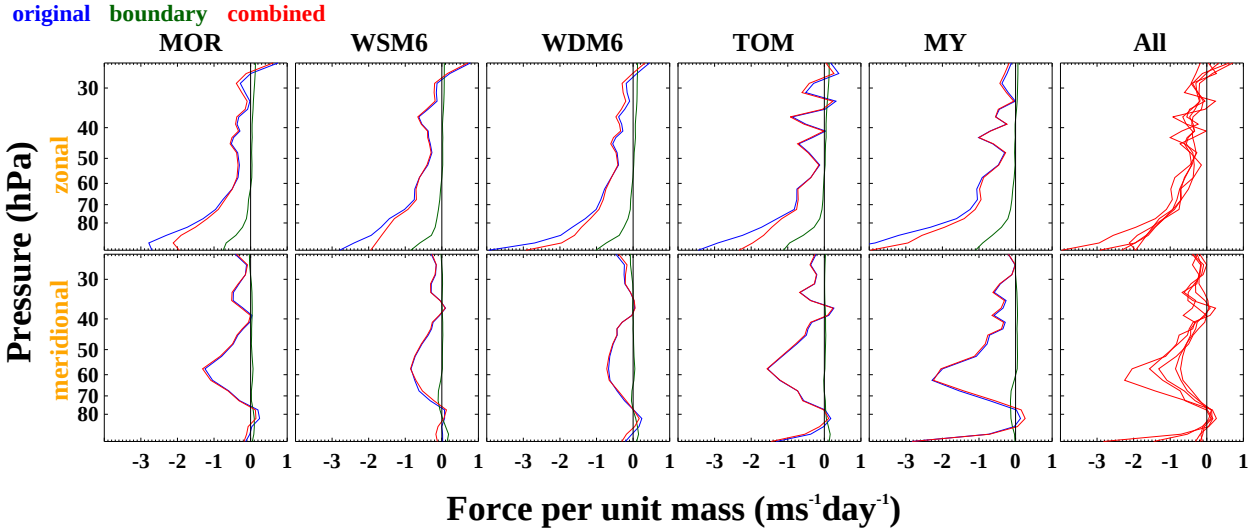

FIG. 9. Zonal (top row) and meridional (bottom row) ensemble-mean forcing with boundary flux corrections. All lines represent 5-hour inner-domain averages. The forcing as calculated from the vertical momentum flux profiles is shown in blue. The green curve indicates the boundary flux contribution due to waves that leave the domain and the red curve shows the net force. For better comparison the net force curves of all ensembles are overlaid in the rightmost diagram. Three-point triangular smoothing has been applied.

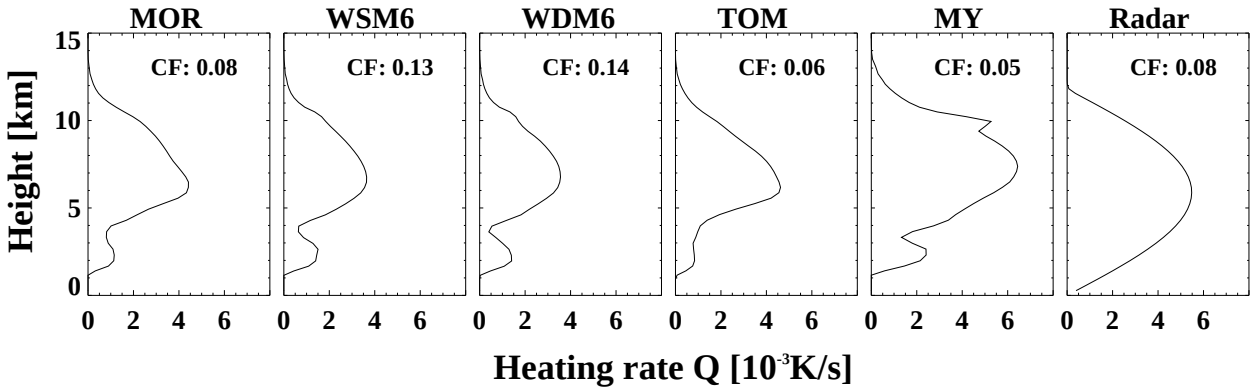

FIG. 10. Ensemble-mean vertical heating rate profiles averaged over all convective pixels and the time interval 3:10-5:10 UTC. We define a grid point as convective when the 10-min heating exceeds .004 K/s anywhere in the column. The convection fraction (CF) shown in the diagram is defined as the fraction of the domain that exceeds this threshold. All graphs are based on a horizontal resolution of 1 km. The radar profile is calculated using estimated values for the maximum heating amplitude and the heating height h as explained in section 5. The radar profile has the half-sine shape that is assumed in the Beres parameterization.

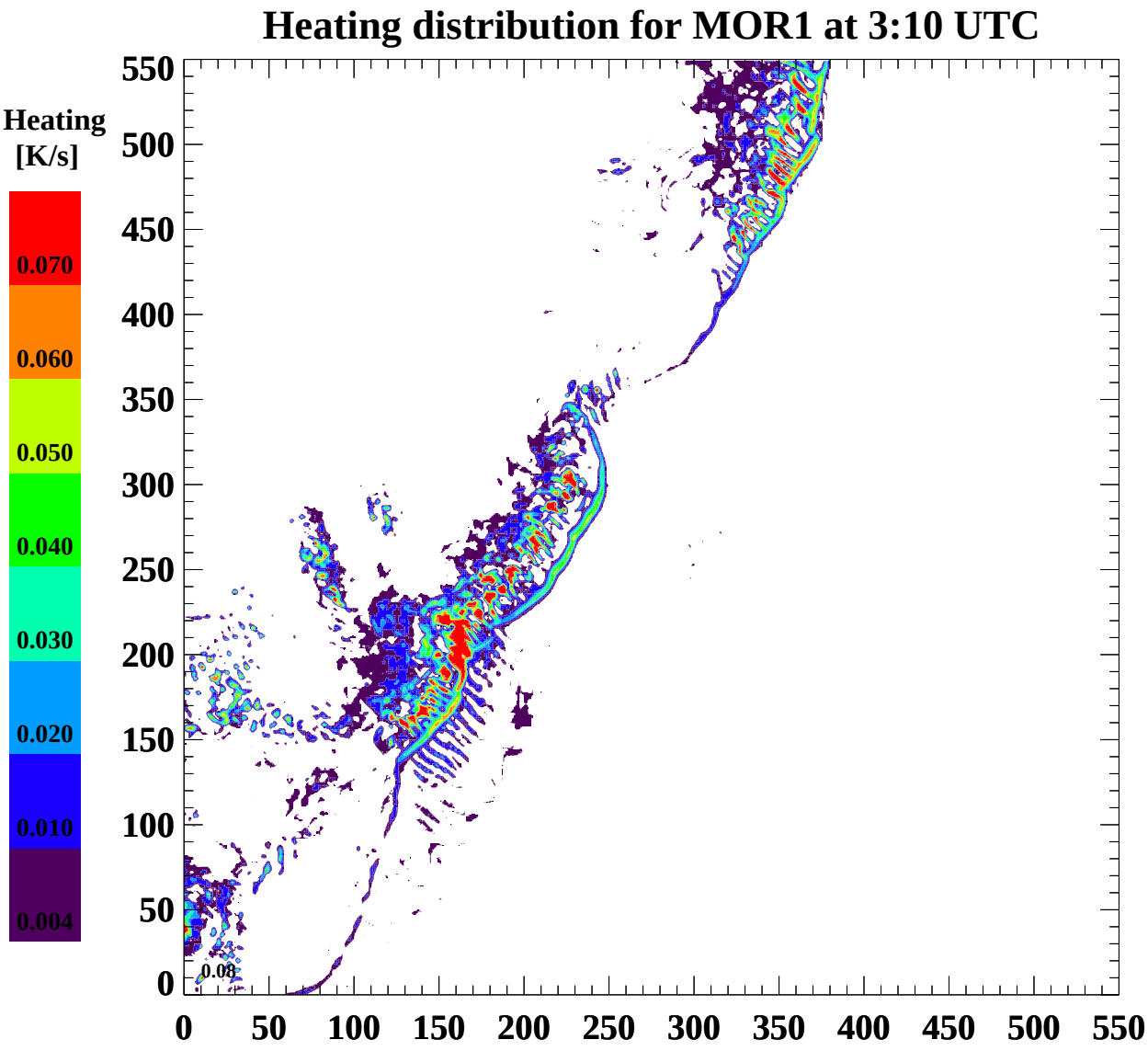

FIG. 11. Map of heating rates exceeding the convective threshold of .004 K/s. Shown is the 550 km×550 km large area of the innermost domain (see Appendix A). Colors display the maximum heating in the column over each 1 km×1 km grid cell.

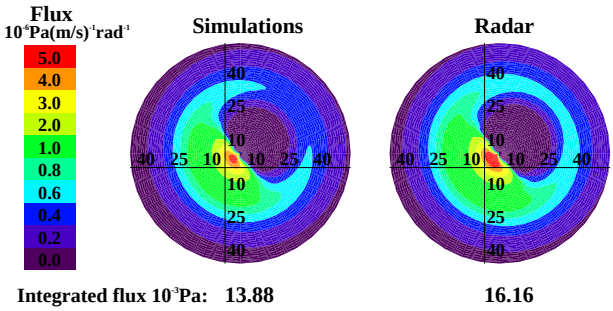

FIG. 12. Momentum flux spectra as a function of phase speed in m/s (radial coordinate) and propagation angle produced by the Beres parameterization. The left diagram results from using information about the simulated heating fields as input to the parameterization and displays the spectrum averaged over all simulations. Integrated flux values range from 7.14 mPa to 30.77 mPa among the simulations. The right diagram results from applying the parameterization to radar measurements. The angular resolution is 10° and the resolution in phase speed is 1 m/s.

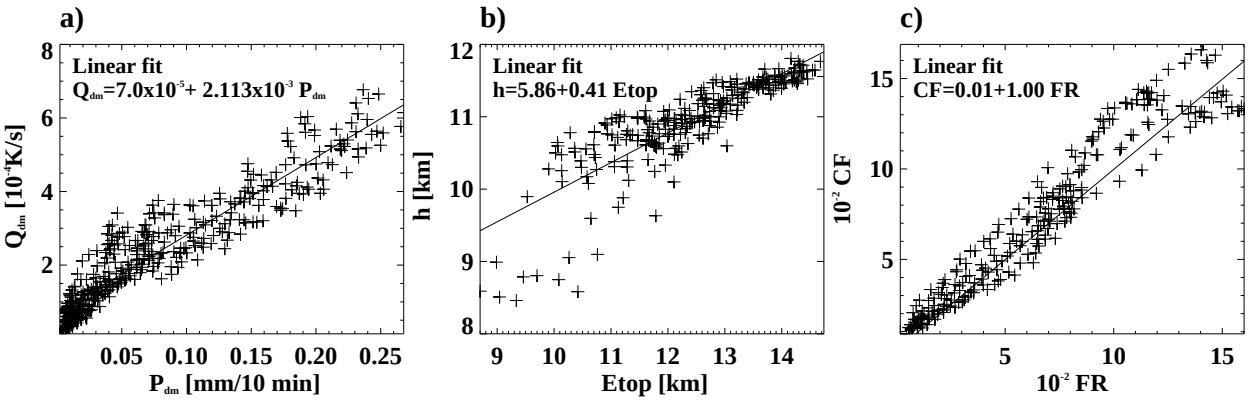

FIG. 13. Scatter plots showing 10 minute data from all or selected simulations (see text). Panel a shows the relationship between domain mean precipitation (P_{dm}) and the maximum of the convective vertical heating profile multiplied by the convective fraction ($Q_{max} \times CF \equiv Q_{dm}$). Panel b shows the relationship between the heating depth (h) and the average over the 0.1% of the highest echo tops (Etop). Panel c shows the relationship between convective fraction (CF) and fraction of raining pixels (FR) with precipitation rates greater than 0.17 mm/10 minute. The straight lines are linear fits. The rain threshold of 0.17 mm/10 minutes in panel c (based on a resolution of 8 km ×8 km) is chosen to obtain a slope of one for the linear fit. The linear fits are used to obtain parameterization input parameters (h, CF, and Q_{dm}) from 8 km× 8 km radar precipitation and echo top fields. More information on the definition of CF, h and Q_{max} can be found in the text.

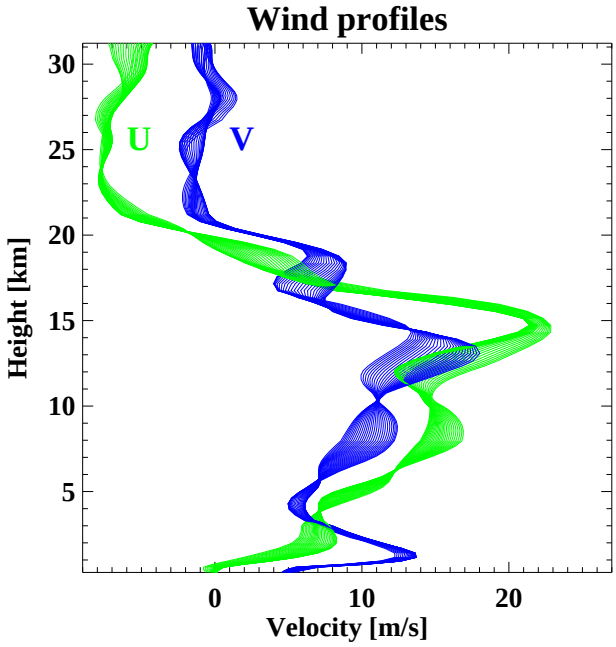

FIG. 14. Domain-mean zonal and meridional wind profiles at 10 min intervals averaged over all simulations. These are used to calculate the winds in and above the heating region as input to the Beres parameterization for the "Radar" spectrum in Fig. 12.